# Supporting Information

## Table of Contents

## Note S1: Comparison of C 1s fits obtained by Python-based or manual fitting

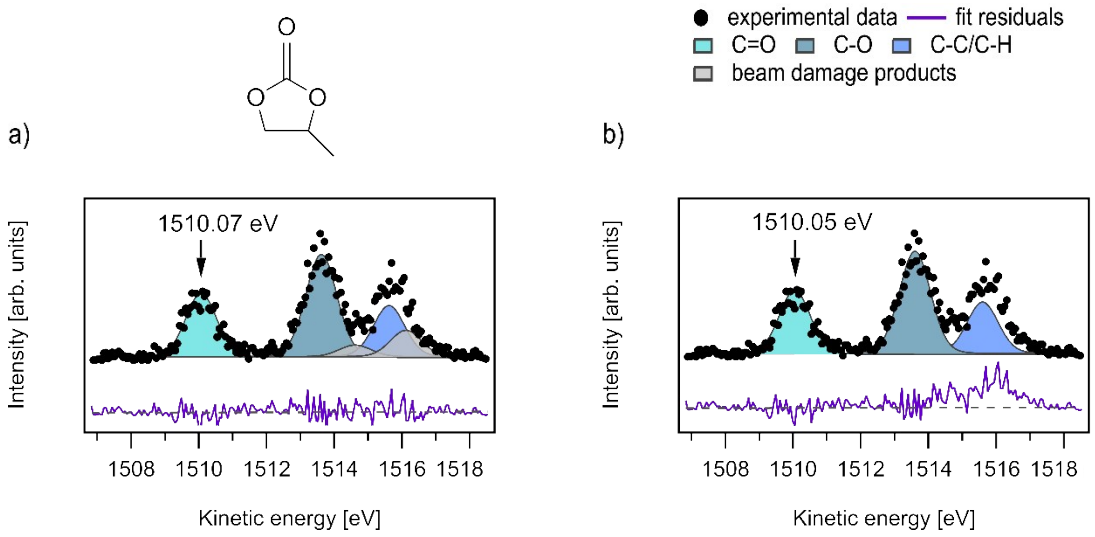


**Figure S1.** Fast acquisition C 1s spectrum of the electrolyte recorded during spectroelectrochemical experiments (black dots) fitted in two ways: a) manually fit and b) fit using the Python script. Chemical environments assigned to the fitted peaks are given in the legend. Kinetic energy of the C=O peak is displayed above the arrow pointing to the C=O peak. Residuals (violet curve) are displayed beneath the fitted spectra and the dashed grey line marks a zero residual.

Manual fit and Python-based fit of the electrolyte C 1s spectrum are displayed in Figure S1. The main three peaks (blue or green colours) correspond to the three different carbon environments present in PC (solvent). The two grey peaks were observed to grow under prolonged irradiation of a single measuring spot and were hence attributed to the beam damage products. Chemical composition of the beam damage products was not determined and the intensity of the beam damage peaks was minimized by continuously scanning along the meniscus surface while acquiring C 1s photoelectron spectra.

When interpreting spectroelectrochemical experiments, C 1s fitting was necessary to determine PC peak position ($KE$) with sufficient accuracy. Beam damage peaks were, in Python-based fits, neglected and the goodness of fit was judged based on the overlap between the experimental data and the PC spectrum shape under the C=O peak and the lower $KE$ half of the C-O peak (in Figure S1b kinetic energies from 1513.6 eV downwards).

Reliability of the Python-based fitting was tested against the manually fit C 1s spectra. Since the purpose of fitting was to determine the PC kinetic energy (kinetic energy of any of the three PC peaks), we compared kinetic energy of the C=O peak, $KE_{C=O}$, as obtained from the Python-based fitting and the manual fitting (an example shown in Figure S1). In the given example, $KE_{C=O}$ amounted to 1510.07 eV when fit manually and 1510.05 eV when fit using Python-based script. The difference of 0.02 eV was well-within the desired fitting accuracy. On average, the systematic error from fitting (the

difference in $KE_{C=0}$ obtained with the Python-based and the manual fit) amounted to 0.09 eV. Since we were interested in the change in $KE$, a consistent systematic error did not present a problem for the data interpretation. The random error in $KE_{C=0}$ was calculated from the $KE_{C=0}$ points obtained before applying a potential step, i.e. at the start of a spectroelectrochemical experiment when $KE_{C=0}$ should be a constant value. The random error ($\sigma_E$) in $KE_{C=0}$ obtained for 60 data points amounted to 0.0032 eV and the 95% confidence level calculated as 2.0 $\sigma_E$ was 0.0064 eV. From this, we concluded the random error to be small enough to rely on the use of the Python script for C 1s fitting.

## Note S2: APXPS measuring position

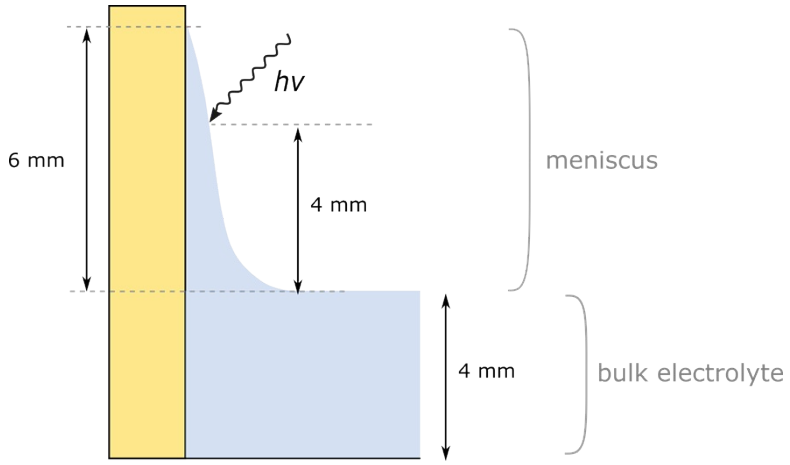


**Figure S2.** Scheme of the WE|electrolyte interface. The total meniscus height, the height of the APXPS measuring position and the depth to which the WE is immersed in the bulk electrolyte are indicated.

## Note S3: APXPS experimental setup

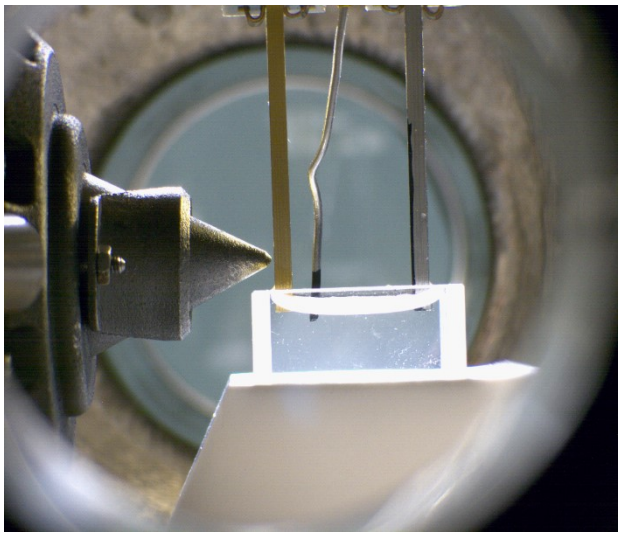

**Figure S3.** Side view of the investigated electrochemical system inside the APXPS analysis chamber. From left to right: Au working electrode, LTO reference electrode and LTO counter electrode immersed into 1 M $LiClO_4$ in a quartz cuvette.

## Note S4: C 1s spectra of PC for different electrolyte compositions

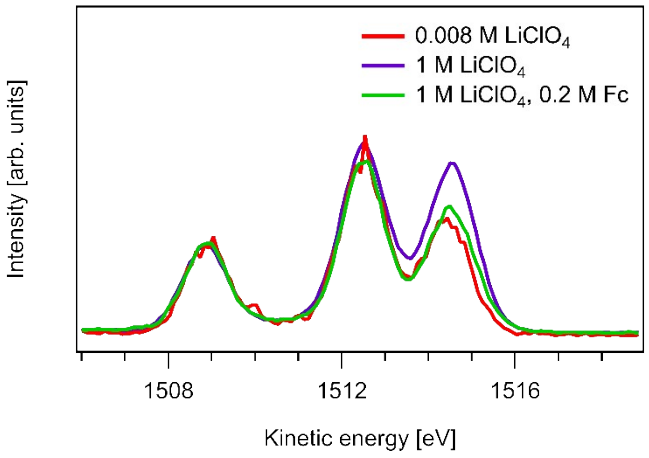


**Figure S4.** C 1s spectra recorded in different electrolyte compositions; PC was the solvent for all three electrolytes. Red and green spectra are scaled on the y-axis to fit on the same plot; the red spectrum intensity is increased by 16-fold and the green spectrum intensity is reduced to 0.0014 of its original value. The spectra differ in their intensity and in their signal-to-noise ratio, because they were recorded under different conditions (detector settings, beam slit width, etc.).

Figure S4 displays C 1s spectra recorded for three distinct electrolyte compositions where an average PC molecule experienced three different chemical environments. Upon inspecting the three C 1s spectra, no shifting in the spectral $KE$ could be observed. The only difference between the spectra is the relative intensity of the highest $KE$ peak (C-C/C-H peak). This is ascribed to different amounts of the beam damage products formed. The amount of the beam damage products depends on the measurement conditions such as photon flux and the duration of irradiation at each measurement spot. Hence, the spectrum recorded using the lowest photon intensity and the shortest dwell time (red spectrum) has the smallest ratio between the C-C/C-H peak intensity and the C=O peak intensity. These measurement settings are also reflected in the spectrum having the lowest signal-to-noise spectrum.

Importantly, no shift in $KE$ meant that the energy levels of C 1s core level electrons remained very similar for all three electrolyte compositions. In other words, the changes in the chemical environment of a PC molecule had a negligible effect on C 1s core level electrons. The three electrolytes differed in their Fc and $LiClO_4$ concentration, which are also the changes expected to occur during electrochemical processes (faradaic and capacitive processes) in proximity of the working electrode. Since such changes of the electrolyte composition did not affect C 1s spectra, we could be confident that the changes in C 1s peak position ($KE$) observed in the experiments presented in this work stemmed from changes in the electrostatic potential and not the changes of the local environment of a PC molecule. Additional explanation relating $KE$ to the electrostatic potential drop across WE|electrolyte interface is given in Note S5.

## Note S5: Probing changes in electrostatic potential drop across electrode/electrolyte interface with APXPS

The ability of (AP)XPS to deduce changes in the electrostatic potential difference across the electrode|electrolyte interface stems from the fact that the photoelectron $KE$ is dependent on the electrostatic potential difference between the electrolyte and the analyzer. Contacted grounded electrode and electrolyte have some electrostatic potential difference $\delta\phi$ established between them. Fermi level of the grounded electrode is aligned with the Fermi level of the (equally grounded) spectrometer analyzer. Since all photoelectron kinetic energies are referenced to the spectrometer Fermi level, core level electrons originating from the grounded electrode retain the same kinetic energy independently of the magnitude of the electrostatic potential difference between the electrode and the electrolyte $\delta\phi$.[1,2] Contrastingly, kinetic energy of electrolyte core level photoelectrons depend on the electronic chemical potential $\mu$ and, importantly, also on the electrostatic potential difference between the electrolyte and the electrode $\delta\phi$ (i.e. the work required to bring an electron from the electrolyte to the electrode). This is evident from Eq. 1, where $h\nu$ is the

X-ray photon energy, $\Phi^{spec}$ is the spectrometer work function, *F* is the Faraday constant and *z* is the electron charge number.[2,3]

$$KE = h\nu - (\Phi^{spec} + \mu + z \cdot \delta\phi) \quad (1)$$

Since the photon energy $h\nu$ and the spectrometer work function $\Phi^{spec}$ are typically constant during an experiment, a change in the kinetic energy of the electrolyte core level electrons, $\Delta KE$, is a sum of the change in the electronic chemical potential $\Delta\mu$ and the change in the electronic electrostatic potential $\Delta(\delta\phi)$ (Eq. 2).

$$\Delta KE = \Delta\mu + z \cdot \Delta(\delta\phi) \quad (2)$$

If the probed core level electrons experience minor or no changes in their local environment, the first term in Eq. 2 ($\Delta\mu$) is assumed to be 0 and any change in the measured $KE$ can be ascribed to the change in the electrolyte electrostatic potential. Hence, by following $\Delta KE$ of such core levels, (AP)XPS can be used to determine the changes in the electrostatic potential difference between a grounded electrode and an electrolyte.[4]

## Note S6: Electrochemical, chemical and electrostatic potential of moveable charges

Electrochemical potential of charged species $i$, $\bar{\mu}_i$, is a thermodynamic quantity defined as the work done to add one particle of species $i$ to the system:

$$\bar{\mu}_i = \left(\frac{\partial G}{\partial n_i}\right)_{p,T} \quad (3)$$

where $G$ is the Gibbs enthalpy, $n_i$ is the number of particles of species $i$ and $p$ and $T$ are pressure and temperature, respectively. Electrochemical potential can also be written as the sum of two contributions, the chemical potential $\mu_i$ (potential due to short range interactions) and the electrostatic potential $\phi$ (potential due to long range interactions):

$$\bar{\mu}_i = \mu_i + z_i e_0 \phi \quad (4)$$

where $\mu_i$ is the chemical potential of species $i$, $z_i$ is the charge number of species $i$, $e_0$ is the elementary charge and $\phi$ is the local electrostatic potential.[5,6] In this work, the species of interest $i$ are electrons and electronic electrochemical, electrostatic and chemical potentials are discussed.

## Note S7: Bulk model 1 (for capacitive processes)

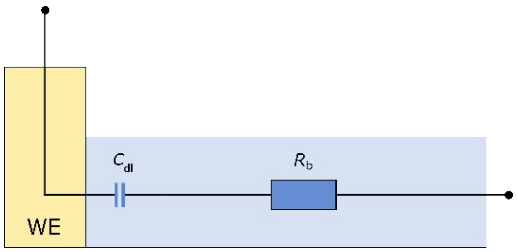


**Figure S5.** Electric circuit representing the bulk model for a system with only charging processes ("bulk model 1").

Current transient expected for ideally polarizable electrode in an electrochemical system with only bulk electrolyte (no meniscus) was obtained from a simple electric circuit model (Figure S5). The circuit consists of two elements, a resistor $R_b$ and a capacitor $C_{dl}$. $R_b$ corresponds to the bulk electrolyte resistance and $C_{dl}$ to the electric double layer capacitance. This circuit is the bulk electrolyte model for a system with only charging processes. When applying a potential step $E$, the expected current response is:

$$i = \left(\frac{E}{R_b}\right) e^{-t/R_b C_{dl}} \tag{5}$$

## Note S8: Fitting with meniscus model 1

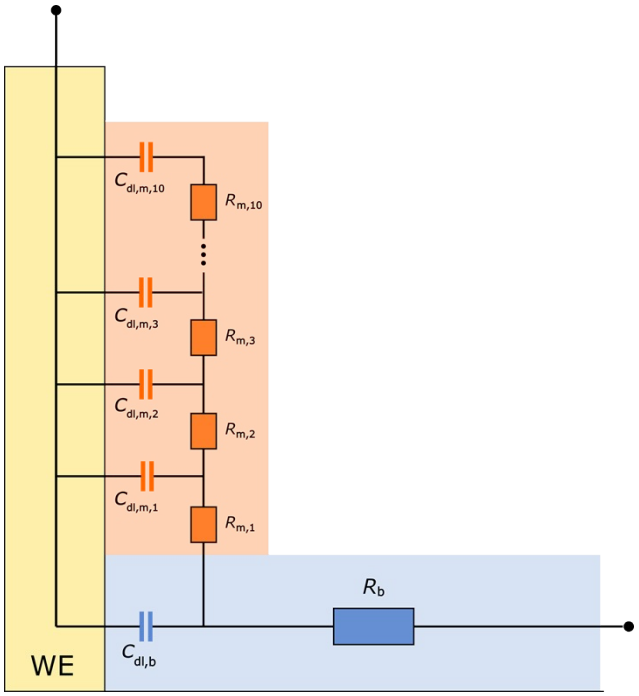


**Figure S6.** Electric circuit representation of the investigated system, which specifically accounts for the particular geometry of the system. The model describes charging processes and is in the text referred to as "meniscus model 1".

Fitting of the current transient obtained for purely capacitive processes was done using the model shown in Figure S6 (also displayed in the main paper in Figure 2d). In addition to the bulk electrolyte resistance $R_b$ and double layer capacitance of the electrode immersed into the bulk electrolyte $C_{dl}$, a ladder-like structure consisting of 10 resistors $R_{m,n}$ and 10 capacitors $C_{dl,m,n}$ was added to the circuit model to simulate the response of the electrolyte meniscus. This transmission line model (TLM) was fit to the experimental data using the following constraints. The meniscus resistors and capacitors with $n = 4,..10$ (above $R_{m,3}$ and $C_{dl,m,3}$) were constrained to have the same resistance and capacitance value as $R_{m,3}$ and $C_{dl,m,3}$, respectively. This constraint was imposed to afford a more stable fit. Additionally, the values of $R_{m,1}$ and $R_{m,2}$ had to be lower than $R_{m,3}$. 10 $RC$ couples in the meniscus ladder were deemed sufficient for a good fit, since reducing the number of $RC$ couples from 10 to 5 still yielded a satisfactory fit of the experimental data. Accuracy of the fitted resistor values was additionally supported by $R_b$ (fitted value 100 Ω) being in good agreement with the bulk electrolyte resistance of 130 Ω estimated from cyclic voltammetry.[7] Sensitivity of the current transient to the values of $R_{m,n}$ resistors and $C_{dl,m,n}$ capacitors (see meniscus model 1 in Figure 2d in the main text) could be estimated by comparing current transients obtained with three distinct sets of $R_{m,n}$ and $C_{dl,m,n}$ values (Figure S7). The red curve was obtained by fitting the experimental current transient with meniscus model 1, yielding $R_{m,n}$ resistance values displayed in Figure 4a in the main text. The

green curve was simulated using meniscus model 1, where each of the meniscus resistors $R_{m,n}$ had a resistance of 500 Ω and capacitors $C_{dl,m,n}$ had the same capacitance values as displayed in Figure 4a in the main text. Finally, the orange current transient was obtained by setting each $R_{m,n}$ resistance to 500 Ω and each $C_{dl,m,n}$ capacitance to 80 µF. Capacitance of 80 µF was chosen since it corresponds to the meniscus having the same specific capacitance (capacitance per surface area) as the bulk electrolyte. This was calculated from the meniscus-to-bulk electrolyte surface area ratio and the bulk electrolyte capacitance of 27 µF obtained by fitting the meniscus model 1 to the experimental data.

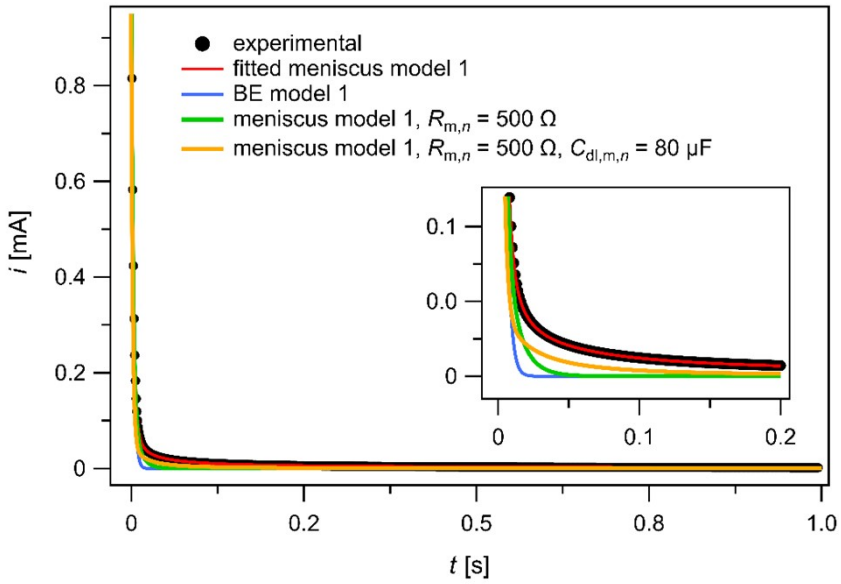


**Figure S7**: Experimental current transient for a potential step from $E_0$ to $E_1$ in the absence of Fc (capacitive process) is displayed with black dots (same as black dots in Figure 2c). Red curve corresponds to the transient obtained by fitting meniscus model 1 to the experimental data (same transient shown with red curve in Figure 2c). Green and orange curve correspond to current transients obtained from simulations with meniscus model 1 where all resistor values $R_{m,n}$ are set to 500 Ω and two distinct sets of $C_{dl,m,n}$ values are used (details in the text above). Blue curve is the best fit of the experimental data obtained with the bulk model 1, which is equivalent to having all $R_{m,n}$ values set to 0. Inset zooms in to the time interval with the largest differences between the three transients.

## Note S9: Faradaic current transient

In order to simulate the faradaic current transient, it is not sufficient to correct the meniscus model 1 only for the reaction current ("meniscus model 2" in Figure 2e and Note S10, SI). Instead, diffusion of

the redox-active species (Fc and $Fc^+$) must be taken into account to simulate the long relaxation times. Interestingly, even the basic bulk electrolyte model which considers Cottrell-like diffusion in conjunction with the Butler-Volmer reaction for the redox reaction[6] and which neglects any meniscus effects ("bulk model 1.1", Note S11 in SI), gives a very good fit of the experimental data (violet curve in Figure S8a). Although a good fit could be obtained using the bulk model 1.1, the value of the fitted diffusion coefficient for Fc, $D_{Fc}$, is about $10^{-8}$ $cm^2/s$, which is roughly two orders of magnitude too small compared to the literature data.[8,9] This suggested that bulk model 1.1 could not describe the investigated system in a satisfactory manner. The error in the value of $D_{Fc}$ can be effectively eliminated by extending the model to also consider the other major contribution to transport, namely, migration ("bulk model 2", see Note S12). Bulk model 2 appears to be satisfactory, both in terms of goodness of fit and correct prediction of the values of the model parameters. This may seem unexpected, as the bulk model 2 does not account for the particular geometry of the meniscus, potentially indicating that the majority of the faradaic current originates in the bulk electrolyte. To learn more of the meniscus contribution to the faradaic current transient, bulk model 2 was employed to investigate effects of a considerable electrolyte ohmic resistance (e.g. resistance along the meniscus) on the transport-reaction behavior. Current transients were simulated for three distinct values of the electrolyte resistance $R_{ele}$ (relation between $R_{ele}$ and $R_b$ is elaborated in Note S13 in SI). As clearly seen in Figure S8b, an increase in $R_{ele}$ results in a decrease of the current magnitude at very short times as well as a decrease in the steady state current. The current transient simulated for 100-fold increase of $R_{ele}$ (red curve) corresponds approximately to the meniscus contribution to the overall current (for details regarding the value of $R_{ele}$, see Note S12) and is observed to be much lower in its magnitude than the current transient simulated for the electrolyte resistance $R_{ele}$ (violet curve). Based on the outlined analysis, we concluded that the current generated in the meniscus in the presence of the $Fc^+$/Fc redox species is negligible compared to the current flowing in the bulk part of the system. A list of all models employed in the analysis and their key properties is given in Note S15.

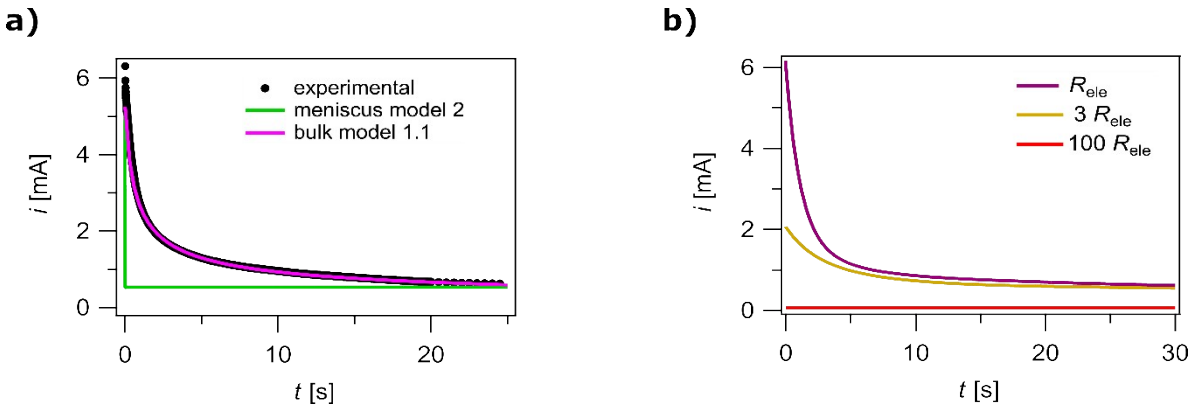


**Figure S8.** a) Chronoamperometric response for a potential step from $E_0$ to $E_2$ (black dots) with 0.2 M Fc in the electrolyte. Green curve represents best fit of the experimental data using meniscus model 2. Pink curve corresponds to the best fit obtained with bulk model 1.1. Black dotted data points and the green curve are the same as plotted in Figure 2e in the main text. b) Current transients simulated using bulk model 2 for three distinct electrolyte resistances $R_{ele}$. Violet curve is the best fit of the experimental transient (dotted curve in 2e) with bulk model 2.

## Note S10: Meniscus model 2 – meniscus model for faradaic processes

In the case of faradaic reaction, the basic meniscus model 1 (see Figure 2d in the main text and Note S8 in SI) needs to be upgraded. The obvious upgrade is to add resistors reflecting the charge transfer (in our case redox) reaction, $R_{ct,i}$ (Figure S9). These resistors are potential dependent as predicted by the Butler-Volmer reaction. A typical simulation obtained using this model is shown in Figure 2e in the main article (green curve). In this simulation all the parameters of the basic meniscus model 1 shown in Figure 2d of the main article remained the same as in the fit shown in Figure 2c (red curve, fitted element values shown in Figure 4a). The current simulated for long times was constrained to match the experimental steady state current, whereas the values for $R_{ct,i}$ were optimized through a curve fitting procedure. We can see in Figure 2e of the main article that such a model cannot reproduce the long relaxation times of the measured curve (Figure 2e, black points). To account for those long relaxation times one needs to introduce diffusion of the active species participating in the redox reaction (see Notes S9 and S12).

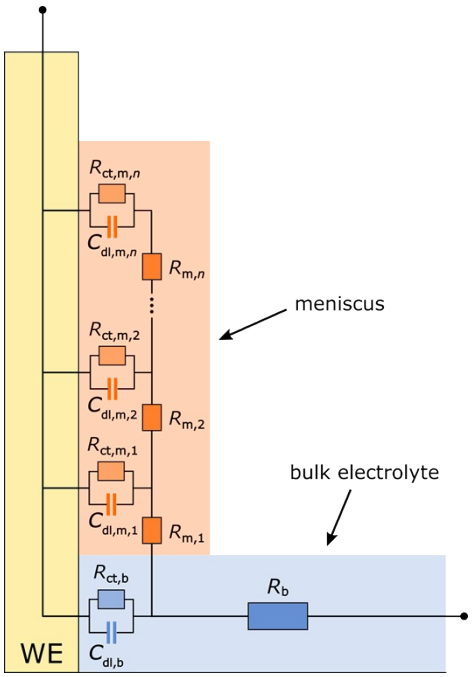


**Figure S9.** Meniscus model 2 (upgraded meniscus model) that accounts for faradaic processes (in addition to the charging processes incorporated in the meniscus model 1). Meniscus model 2 differs from the meniscus model 1 by the inclusion of charge transfer resistors in the bulk electrolyte $R_{ct,b}$ and in the meniscus $R_{ct,m,n}$.

Diffusion is not described in the meniscus model 2. The reason for this is the fitting approach employed in this work. Namely, our goal was to fit $i(t)$ using the simplest model possible. Since a satisfactory fit could already be obtained using the bulk model 2 (see Note S12), we could conclude that the meniscus only had a negligible contribution to the overall current response in the presence of faradaic processes. Hence, there was no need to construct a more sophisticated model (i.e. a meniscus model that would also include diffusion).

## Note S11: Bulk model 1.1

Bulk model 1.1 is based on Fick's laws of diffusion with Butler-Volmer boundary conditions. Differential equations are solved numerically using Electrokitty simulator; the simulator is written in Python and is available on Github, https://github.com/RedrumKid/ElectroKitty. Only the bulk electrolyte geometry is considered in simulations (planar diffusion is assumed). Essentially, bulk model 1.1 describes Cottrell-like diffusion in conjunction with Butler-Volmer kinetics.[6] A good match of the simulated current transient with the experimental data could be obtained by employing the following parameter values in simulations: $A$ = 2 cm$^2$, $k_0$ = 10$^{-6}$ m/s, $c_O$ = 0.2 mol/L and $D_{Fc}$ = 7.5 · 10$^{-8}$ cm$^2$/s, where $A$ is the electrode surface, $k_0$ is the standard heterogeneous rate constant, $c_O$ is the oxidant concentration and $D_{Fc}$ is ferrocene diffusion coefficient. The experimental and the simulated current transients are shown as the dotted black curve and the pink curve in Figure S8a, respectively.

For more details regarding the simulations, we refer the reader to the Electrokitty repository on Github.

## Note S12: Bulk model 2

In terms of transmission line model (TLM), diffusional processes can be represented by introducing chemical capacitors.[10] As diffusional processes are much slower than migration or reaction, it can be assumed that introducing diffusion already in the bulk model will generate relaxation times on the order of tens of seconds which are typical relaxation times observed in the actual measurement such as shown in Figure 2e (black dots). A typical transmission line model for bulk diffusion combined with charge transfer reaction[10] and including electrolyte resistance, $R_{ele}$, is shown in Figure S10. In creating this model, we used the following assumptions: (i) the diffusion layer is of finite length (determined by electrolyte convection), (ii) the electrolyte thickness (distance to reference electrode) is much bigger than the thickness of the convection-limited diffusion layer, which is around 100 µm, (iii) the transport number of the active species is considerably larger than 0. As a result of (iii), the values of the resistors in the »inactive« rail ($R_i$) cannot be approximated as 0 (by contrast, conventional models based on the Cottrell equation assume that the transport number of active species is 0 and the value of $R_i$ is also 0).

Unlike bulk model 1.1, bulk model 2 does consider migration of mobile ions in the bulk electrolyte phase (between the working and counter electrode) and its effects on the current transient. Specifically, the coupled electrolyte migration and diffusion inside diffusion layer are modelled through the magnitude and the topology of $R_{ele}$ and the distributed elements $R_a$, $R_i$ and $C_{chem}$. Bulk model 2 shown in Figure S10 contains 6 independent parameters which means that it is overparametrized with respect to the shape of the measured curve (the measured curve can be fitted using 3 parameters only). By keeping the values of $R_{ele}$, $C_{dl,i}$, $C_{dl,a}$ and $R_{ct}$ in a value range that was physically reasonable (based on this work and/or the literature) when fitting bulk model 2 to the experimental data, the right order of magnitude of the fitted $D_{Fc}$ could be obtained. The fit is shown in Figure 2e in the main text (orange curve).

After obtaining a satisfactory fit, we concluded that bulk model 2 was successful at describing the key processes determining the current transient although it could not provide unique values of the corresponding parameters due to overparametrization. Still, having a consistent model enabled us to employ bulk model 2 to effectively predict selected trends, e.g. changes in the current transient due to a change in the magnitude of $R_{ele}$ as shown in Figure S8b. Briefly, since the main difference between the meniscus and the bulk electrolyte is in the magnitude of $R_{ele}$ or $R_b$ (relation between $R_{ele}$ and $R_b$ elaborated in Note S13), the trends obtained for an increasing electrolyte resistance $R_{ele}$ are

informative of the meniscus faradaic response. The trends show that, following the enormous meniscus resistance, the current generated in the meniscus in the presence of reaction-diffusion of active species is negligibly small compared to the current in the bulk part of the system.

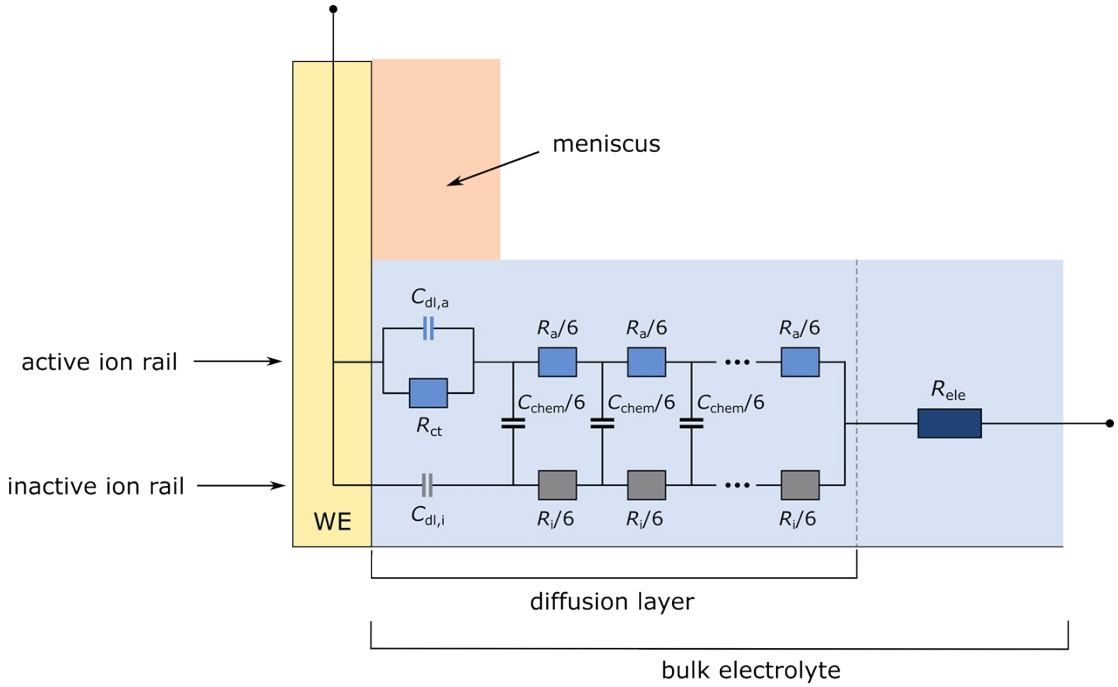


**Figure S10.** Electric circuit representing bulk model 2.

We note that an even more accurate description of the experimental system would be obtained if the model contained a description of all on-going processes (migration, diffusion, charge transfer) not only in the bulk electrolyte but also in the meniscus. However, the aim of fitting faradaic $i(t)$ was to identify the simplest model that could adequately reproduce the experimental transients. This approach allowed us to determine which processes dominate the experimental response.

## Note S13: Relation between electrolyte resistances $R_b$ and $R_{ele}$

Bulk model 1 employs resistor $R_b$ to describe the bulk electrolyte resistance, whereas bulk model 2 uses three elements $R_{ele}$, $R_a$ and $R_i$ ($R_a$ and $R_i$ are distributed elements) to describe the same bulk electrolyte resistance. To take this distinction into account, $R_b$ is referred to as the bulk electrolyte resistance in this work, while $R_{ele}$ is referred to as the electrolyte resistance. The difference in their physical meaning is clearly evident from the topology of the models presented in this work. The three elements $R_{ele}$, $R_a$ and $R_i$ can be linked to $R_b$ according to the expression:

$$R_b = \frac{R_a R_i}{R_a + R_i} + R_{ele} \quad (7)$$

In bulk model 2, the magnitude of $R_a$ and $R_i$ is dependent on the diffusion layer thickness. In our experiments, the diffusion layer thickness is much smaller than the distance between the WE and the CE due to the relatively short measurement times and due to diffusion layer thickness being limited by convection. As a result, the first term in Eq. 7 could in some instances be neglected, thus yielding $R_b \approx R_{ele}$. In simulations presented in this work, the same value (100 Ω) was used for $R_{ele}$ and $R_b$ since the error due this approximation was deemed to be smaller than other experimental and fitting errors.

## Note S14: Bulk electrolyte resistance

Bulk electrolyte resistance $R_b$ of 1 M $LiClO_4$ was estimated to be 100 Ω by fitting the meniscus model 1 to the capacitive current transient. In the presence of 0.2 M Fc, the bulk electrolyte resistance estimated from cyclic voltammetry amounted to 130 Ω.[7] Good agreement between the two values increased our confidence in the accuracy of the estimated $R_b$ as well as confirmed that no major change of the bulk electrolyte conductivity took place with the addition of Fc.

## Note S15: List of electrochemical models employed in this work

**Table S1:** Electrochemical models employed in this work and their main properties.

| **Name of the model** | **Model details** | **Segments of the electrolyte considered in the model** |
|---|---|---|
| Meniscus model 1 | TLM description of capacitive processes at the interface. | Meniscus and bulk electrolyte |
| Meniscus model 2 | TLM description of capacitive and faradaic processes at the interface. Diffusional transport not incorporated in the model. | Meniscus and bulk electrolyte |
| Bulk model 1 | Equivalent circuit describing capacitive processes at the interface. | Bulk electrolyte |
| Bulk model 1.1 | Cottrell equation in conjunction with Butler-Volmer kinetics. | Bulk electrolyte |
| Bulk model 2 | Upgrade of bulk models 1 and 1.1. In addition to capacitive processes, the model also describes faradaic processes and finite-length diffusion. Diffusion described with TLM (diffusion layer segment of the model). | Bulk electrolyte |

## Note S16: Zoom-in to shorter times in spectroelectrochemical experiments

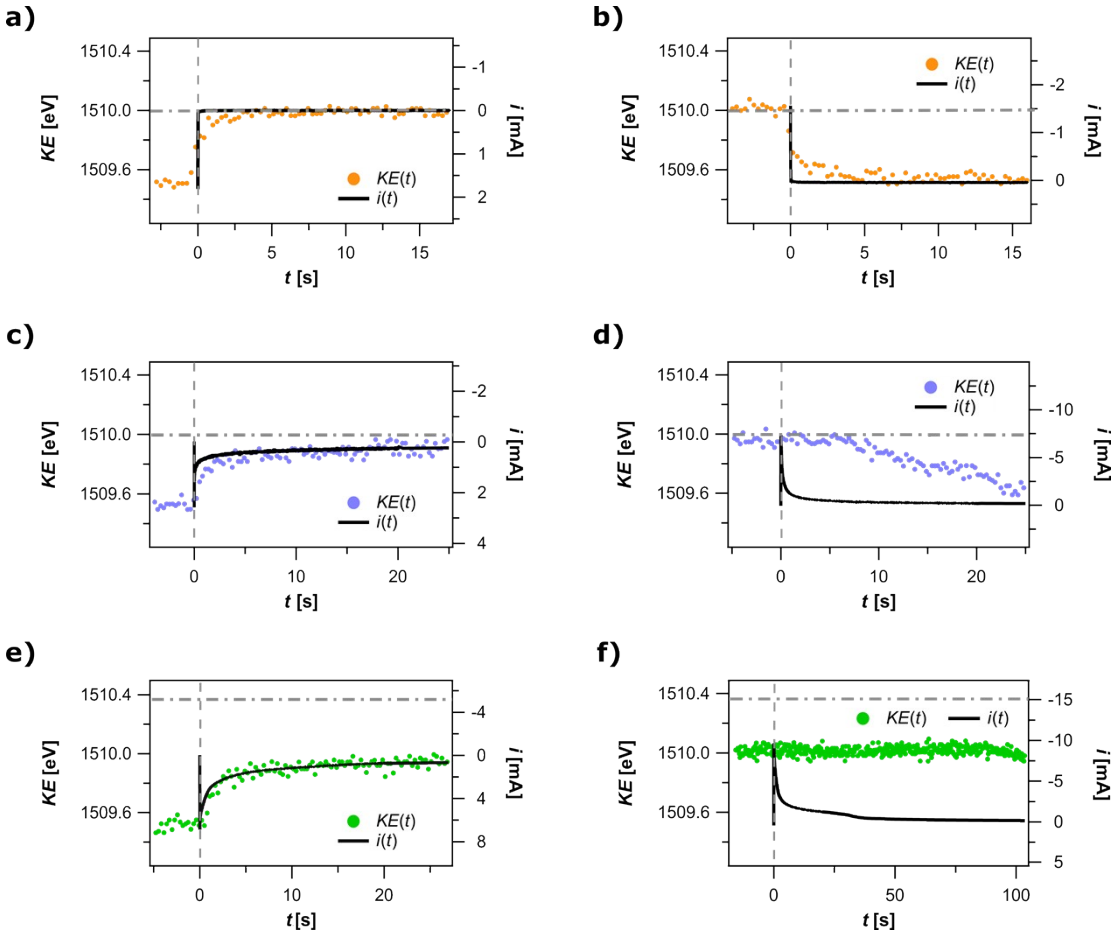


**Figure S11.** Same graphs as in Figure 3 in the main text, but with an enlarged view of the transient current responses. Electric current $i$ (black line) and kinetic energy $KE$ of the C=O peak of C 1s core level (colored dots) as a function of time. Current transient is smoothened for the purpose of clarity. Potential step was initiated at $t$ = 0 s (vertical dashed line). $KE$ expected for 1 eV/V ratio is indicated with a horizontal dashed grey curve. For experimental differences between a-f, see Figure 3 in the main text.

## Note S17: Time delay versus charge transferred in the preceding oxidative step

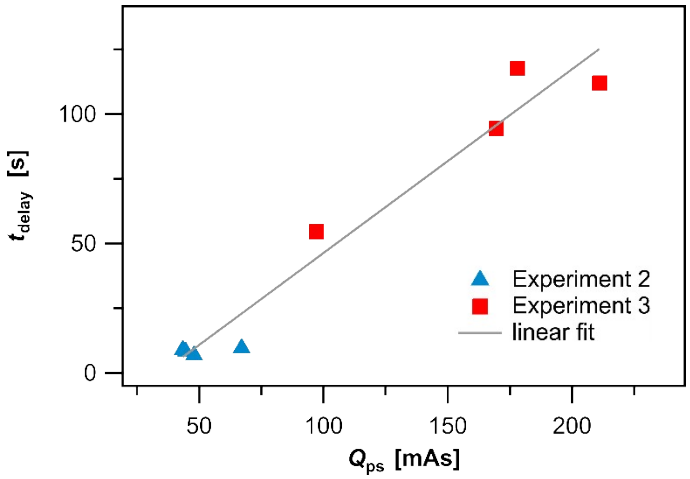


**Figure S12**: Time delay between the potential step and the spectroscopic response, $t_{delay}$, plotted against the amount of charge transferred in the preceding step $Q_{ps}$. The preceding step was an oxidative potential step (a step to higher WE potentials). The time of the spectroscopic response is determined as the time of the onset of $KE$ changing (i.e. the time when $KE$ starts to noticeably change). Linear fit of the data for Experiment 2 (blue triangles) and Experiment 3 (red squares) is shown with a grey line.

## Note S18: Photoelectron spectra of electrolyte species

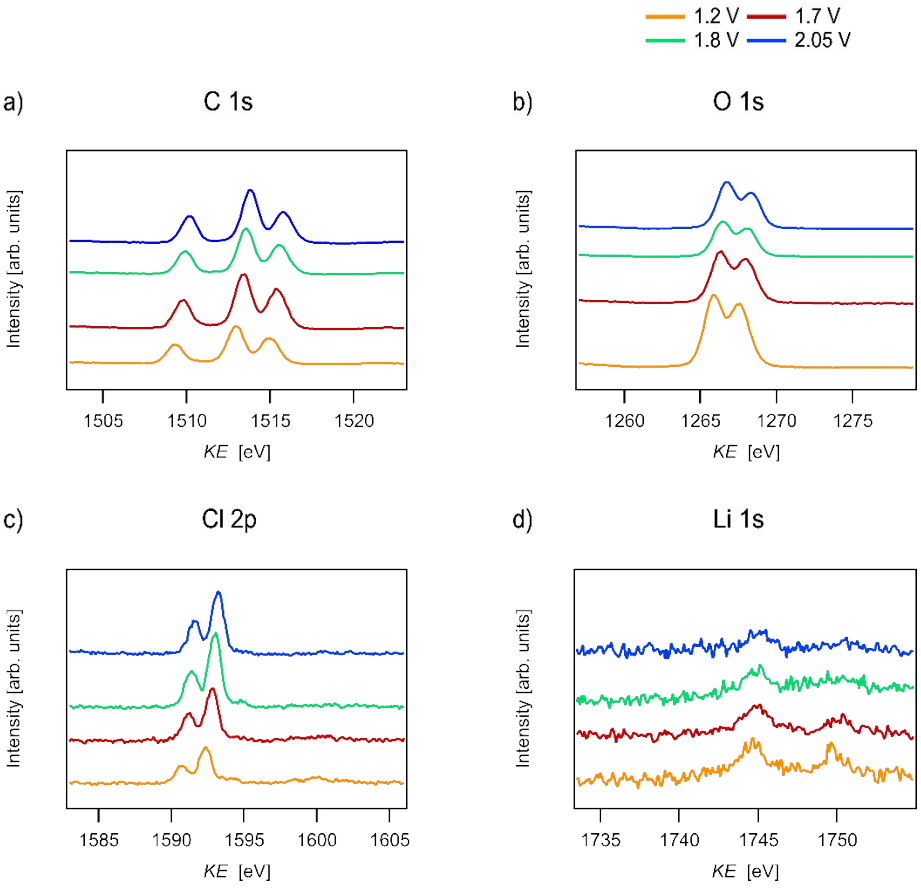


**Figure S13.** Photoelectron spectra of the electrolyte core levels: a) Cl 1s, b) O 1s, c) Cl 2p and d) Li 1s. Each core level was probed at four distinct working electrode potentials. The spectra are not normalized and were collected in scanning detector mode. All spectra shown were acquired after the current in the electrochemical cell decayed to a value below 15 µA.

Core level photoelectron spectra of the electrolyte components (Figure S13) were observed to shift with the working electrode potential. Aside from shifting in their kinetic energy, the spectral shape of C 1s and O 1s remained the same for all working electrode potentials. The spectra of Cl 2p and Li 1s also shifted in their kinetic energy. As for Li 1s spectra, going to lower working electrode potentials resulted in an increased contribution of the peak at ≈1750 eV. This peak was assigned to an impurity, most likely due to a $Mg^{2+}$ species. The increase in $Mg^{2+}$ signal contributions observed when going to lower working electrode potentials could be due to an enhanced surface accumulation of ions brought on by a change in the electrostatic potential drop between the electrolyte and the gas phase. Determining the origin of $Mg^{2+}$ was not within the scope of this work and was hence not explored further.

Kinetic energy shifts of each electrolyte core level as a function of the working electrode potential are shown in Figure S14. Experimentally observed shifts are compared to the theoretically expected $\Delta KE$-to-$\Delta E_{WE}$ ratio of 1 eV/V (black line in Figure S14). $KE$ shifts of C 1s, O 1s and Cl 2p core levels are in good

agreement with the expected 1 eV/V ratio, while a somewhat larger deviation from the expected $KE$ shifts is seen for Li 1s core level. This is most likely caused by the low Li 1s signal-to-noise ratio and the resulting poor accuracy of the peak kinetic energy as determined from the Li 1s spectra. All in all, the satisfactory agreement between the experimentally observed and the theoretically predicted $KE$ shifts confirms that, given small enough current densities, all electrolyte species inside the meniscus experience the same electrostatic potential as in the bulk electrolyte.

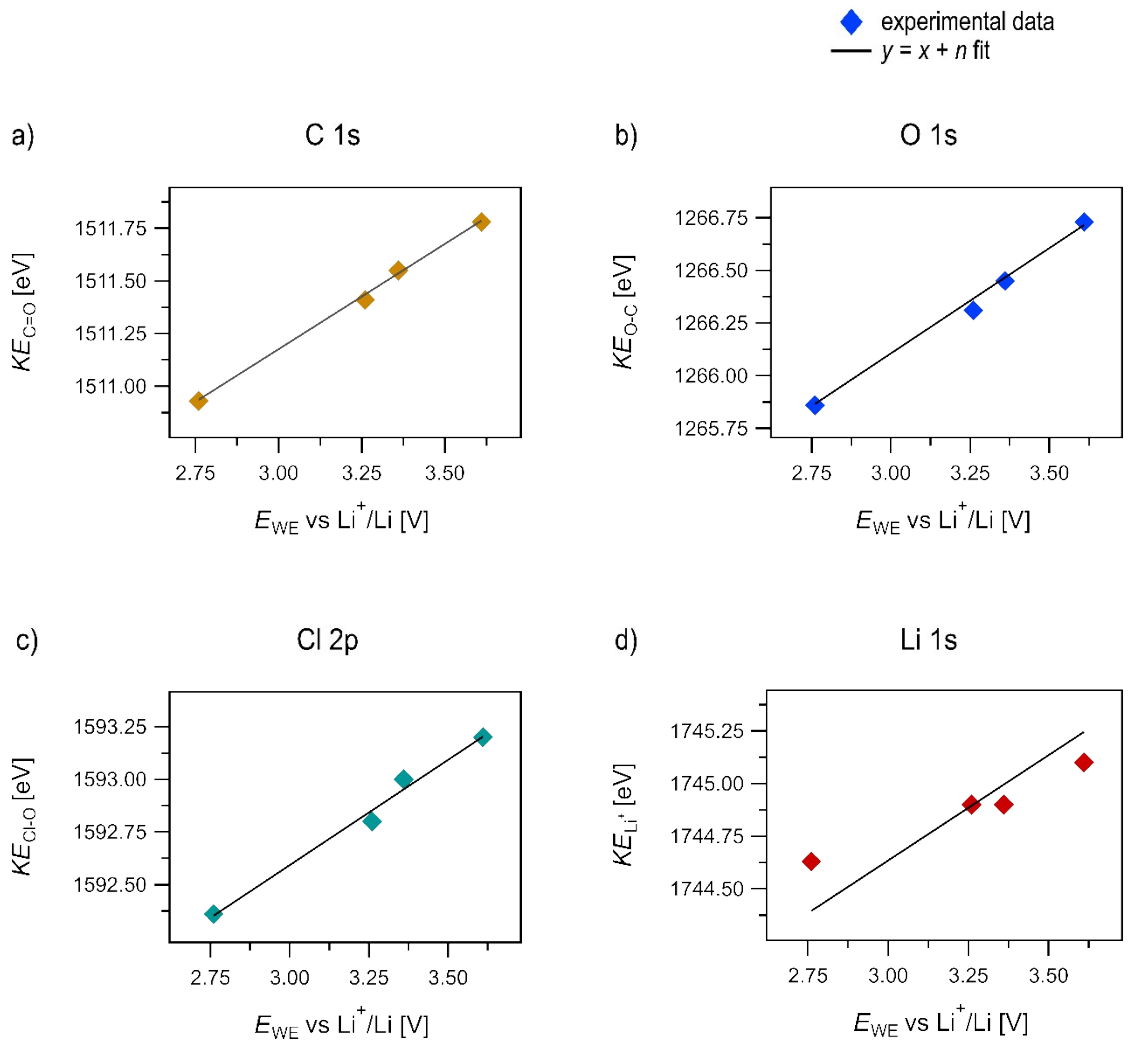


**Figure S14.** Kinetic energy of a) C=O peak in C 1s, b) O-C peak in O 1s, c) Cl-O peak in Cl 2p and d) $Li^+$ peak in Li 1s as a function of the working electrode potential $E_{WE}$. Diamond signs denote the experimentally determined peak kinetic energies, whereas black lines correspond to the best fit using the function $KE = E_{WE} + C$, where $C$ is an arbitrary constant.

## Note S19: Photoelectron spectra of working electrode species

Since both the working electrode and the spectrometer analyzer are grounded, kinetic energies of the photoelectrons originating from the WE and measured at the spectrometer analyzer are expected to remain constant for all WE potentials. This is confirmed by inspecting Au 4f spectra recorded at distinct WE potentials (Figure S15a). Kinetic energy of the main peak in C 1s spectra recorded at the WE surface is also independent of the WE potential (Figure S15b). From this, we can conclude that WE is, in fact, grounded and that the surface layer of carbon-containing species on the WE surface is thin enough to fully adapt to the WE potential (i.e. carbon-containing species behave as grounded).

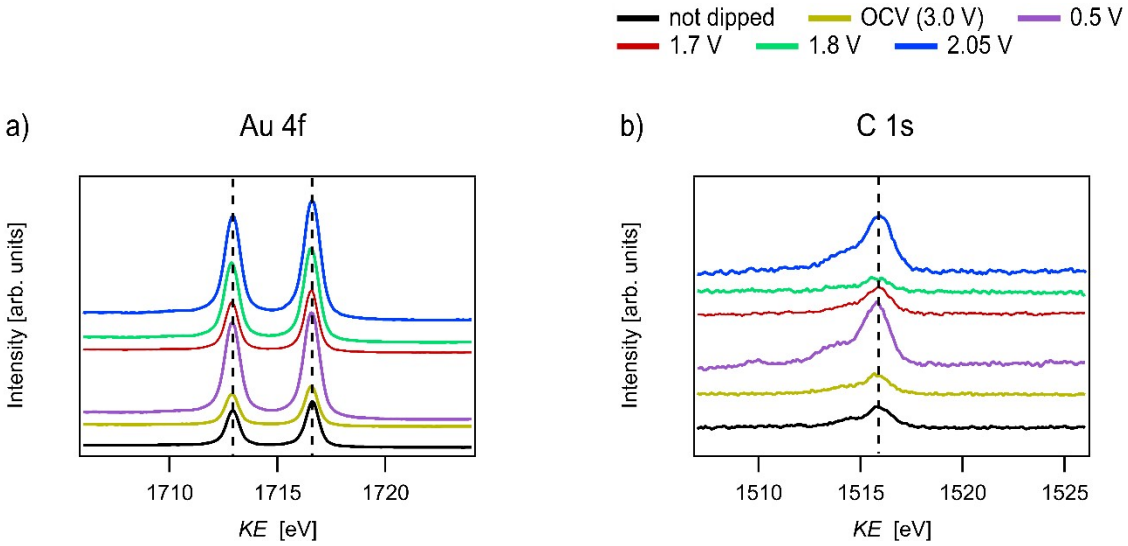


**Figure S15.** Core level spectra of a) Au 4f and b) C 1s recorded before dipping the electrodes in the electrolyte and at five different WE potentials. The absence of any shifts in $KE$ is visualized by the vertical dashed lines running through the center of the two Au 4f peaks and the main C 1s peak at all WE potentials.

## **Note S20:** CA measurements

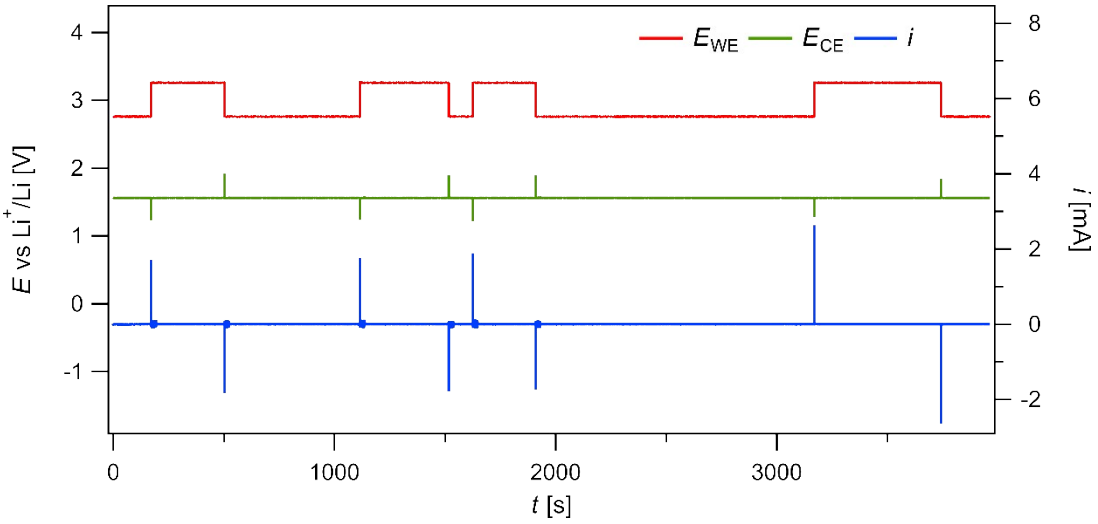


**Figure S16.** A typical CA measurement: working electrode potential $E_{WE}$ (electrochemical system perturbation) and the resulting counter electrode potential $E_{CE}$ and current $i$ (response to the perturbation). The shown data was collected while simultaneously acquiring C 1s spectra (specifically, during Experiment 1, in which the electrolyte only contained the supporting electrolyte and responded to the potential step with double layer charging).

## References


1 M. Favaro, B. Jeong, P. N. Ross, J. Yano, Z. Hussain, Z. Liu and E. J. Crumlin, Unravelling the electrochemical double layer by direct probing of the solid/liquid interface, *Nat. Commun.*, 2016, **7**, 12695.

2 I. Källquist, F. Lindgren, M. T. Lee, A. Shavorskiy, K. Edström, H. Rensmo, L. Nyholm, J. Maibach and M. Hahlin, Probing Electrochemical Potential Differences over the Solid/Liquid Interface in Li-Ion Battery Model Systems, *ACS Appl. Mater. Interfaces*, 2021, **13**, 32989–32996.

3 S. Hüfner, *Photoelectron spectroscopy: principles and applications*, Springer Science & Business Media, 2013.

4 I. Källquist, T. Ericson, F. Lindgren, H. Chen, A. Shavorskiy, J. Maibach and M. Hahlin, Potentials in Li-Ion Batteries Probed by Operando Ambient Pressure Photoelectron Spectroscopy, *ACS Appl. Mater. Interfaces*, 2022, **14**, 6465–6475.

5 W. Schmickler and E. Santos, *Interfacial electrochemistry*, Springer Science & Business Media, 2010.

6 A. J. Bard, L. R. Faulkner and H. S. White, *Electrochemical methods: fundamentals and applications*, John Wiley & Sons, 3rd edn., 2022.

7 A. M. Bond, K. B. Oldham and G. A. Snook, Use of the ferrocene oxidation process to provide both reference electrode potential calibration and a simple measurement (via Semiintegration) of the uncompensated resistance in cyclic voltammetric studies in high-resistance organic solvents, *Anal. Chem.*, 2000, **72**, 3492–3496.

8 J. Reiter, J. Vondrák and Z. Mička, The electrochemical redox processes in PMMA gel electrolytes - Behaviour of transition metal complexes, *Electrochim. Acta*, 2005, **50**, 4469–4476.

9 C. O. Laoire, E. Plichta, M. Hendrickson, S. Mukerjee and K. M. Abraham, Electrochemical studies of ferrocene in a lithium ion conducting organic carbonate electrolyte, *Electrochim. Acta*, 2009, **54**, 6560–6564.

10 J. Jamnik and J. Maier, Generalised equivalent circuits for mass and charge transport: Chemical capacitance and its implications, *Physical Chemistry Chemical Physics*, 2001, **3**, 1668–1678.